# Dynamical Origin of Rebound versus Dissociation Selectivity During Fe-Oxo Mediated C-H Functionalization Reactions

Jyothish Joy, Anthony J. Schaefer, Matthew S. Teynor, and Daniel H. Ess\*

Department of Chemistry and Biochemistry, Brigham Young University, Provo, UT 84604, USA

**Keywords:** Iron-Oxo, C-H Bond Functionalization, Rebound, Dissociation, Machine Learning, Direct Dynamics.

#### ABSTRACT

The mechanism of catalytic C-H functionalization of alkanes by Fe-oxo complexes is often suggested to involve a hydrogen atom transfer (HAT) step with formation of a radical pair intermediate followed by diverging pathways for radical rebound, dissociation, or desaturation. Recently we showed that in some Fe-oxo reactions the radical pair is a nonstatistical type intermediate and dynamic effects control rebound versus dissociation pathway selectivity. However, the effect of solvent cage on the stability and lifetime of the radical pair intermediate has never been analyzed. Moreover, because of the extreme complexity of motion that occurs during dynamics trajectories the underlying physical origin of pathway selectivity has not yet been determined. For the reaction between [(TQA\_Cl)Fe<sup>IV</sup>O]<sup>+</sup> and cyclohexane, here we report explicit solvent trajectories and machine learning analysis on transition-state sampled features (e.g. vibrational, velocity, and geometric) that identified the transferring hydrogen atom kinetic energy as the most important factor controlling rebound versus non-rebound dynamics trajectories, which provides an explanation for our previously proposed dynamic matching effect in fast rebound trajectories that bypass the radical pair intermediate. Manual control of reaction trajectories confirmed the importance of this feature and provides a mechanism to enhance or diminish selectivity for the rebound pathway. This led to a general catalyst design principle and proof-of-principle catalyst design that showcases how to control rebound versus dissociation reaction pathway selectivity.

#### INTRODUCTION

Catalytic C-H functionalization reactions mediated by high valent heme and non-heme Fe-oxo complexes are a large and important class of enzymatic and biomimetic reactions.<sup>1</sup> The generally accepted mechanism for Fe-oxo mediated C-H functionalization involves an initial hydrogen atom transfer (HAT) reaction step leading to the formation of a radical pair intermediate consisting of Fe(OH) and hydrocarbon radicals (Figure 1). Following HAT a second reaction step occurs where the hydrocarbon radical rebounds back to the Fe(OH) to generate a hydroxylated product coordinated to Fe.<sup>1-3</sup> For most Fe-oxo complexes the resulting radical pair intermediate can also undergo dissociation to radical fragments with solvent cage escape,<sup>4</sup> or the Fe(OH) intermediate abstracts another hydrogen from the carbon fragment leading to the formation of an olefin and an Fe(OH<sub>2</sub>) species.<sup>5-7</sup> Typically, experimental and theoretical (density functional theory (DFT) and wave function) analyses assume that the radical pair intermediate is a statistical structure with a lifetime long enough to control the product chemoselectivity, regioselectivity, and stereoselectivity.<sup>8,9</sup>

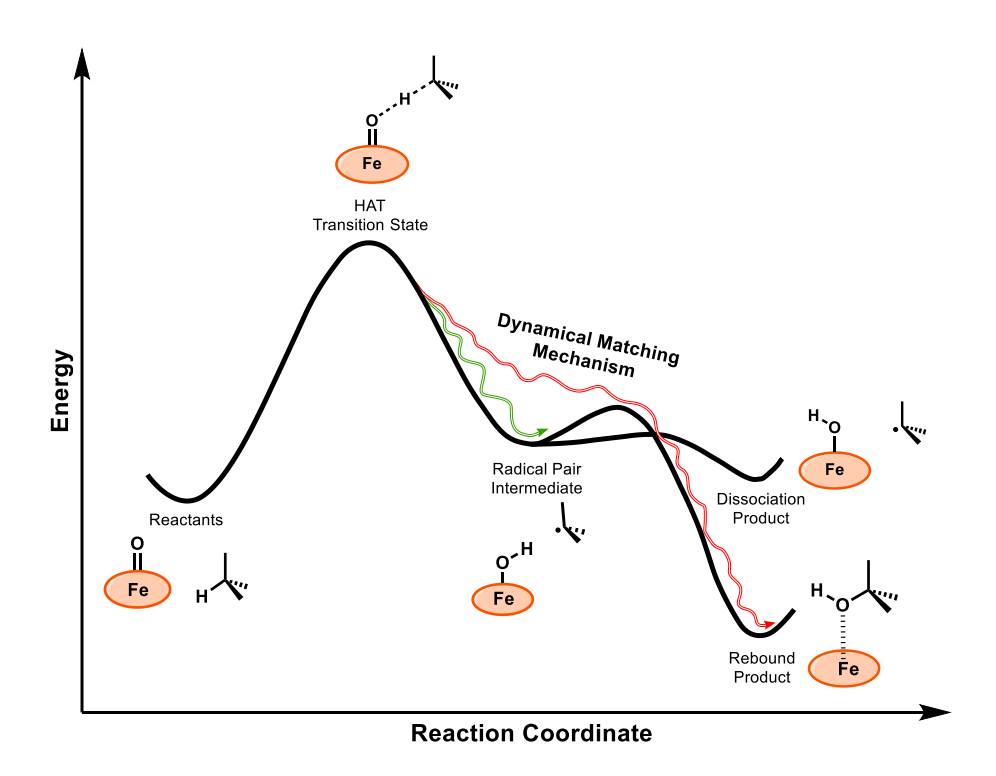


**Figure 1**. Conceptual representation of an Fe-oxo mediated C-H functionalization potential energy landscape (black bold lines) with the radical pair intermediate serves as a branching point for rebound and dissociation pathways. The red arrow represents the dynamical rebound mechanism where trajectories bypass the intermediate structure through a dynamic matching effect. Green pathway represents the radical-pair intermediate forming pathway.

Long-lived radical-pair intermediate in some reactions is essential to explain the radical probe experiments of Groves, 9, 10 and to explain some of the experimental and computational findings from Nam, Que, and Shaik. 4, 11 While several other studies by Newcomb and others suggest that some of these radical-pairs may be very short lived (< 200fs). 12-14 There are also literature precedents for the existence of radical-pair species of intermediate lifetimes (few picoseconds). 15, 16 Recent direct dynamics studies from our group, 17 and later by Houk, 18 have established that the radical pair intermediates in some of these Fe-oxo C-H functionalization reactions are best described as nonstatistical and they do not undergo complete internal vibrational relaxation (IVR) before entering rebound or dissociation pathways. 19, 20 Importantly, our simulations demonstrated that rebound trajectories are nearly concerted, although asynchronous. We also showed that there can be dynamic matching 21, 22 that enables rebound trajectories to bypass the radical pair intermediate type structure and directly rebound (red arrow in Figure 1). 17

While our trajectories revealed a nonstatistical radical pair intermediate and dynamic matching during rebound, the effect of a solvent cage on the dynamic trajectories and the physical origin of the fast rebound versus non-rebound selectivity remains unknown. Understanding the effect of a solvent cage is very important since the solvent could potentially impart a constraint to radical dissociation and/or stabilize the radical-pair intermediate resulting in a longer lifetime. Solvent might also impact the very fast, nearly concerted dynamical process in trajectories with dynamic matching. Also, the underlying physical features at the transition state that guide a trajectory to rebound versus a trajectory to dissociate is unknown. This fundamental physical insight is critical to unveil because it has the potential to directly propel the design of new catalysts with much higher rebound selectivity. Importantly, understanding and predicting the outcome of deterministic trajectories based on initial conditions is nontrivial due to highly complex multi-dimensional energy landscapes with forces at the transition state and forces along the descent to intermediates or products. Therefore, to this point our goal was to use machine learning to analyze transition-state features (vibrational, velocity, and geometric) to identify the origin of rebound versus non-rebound pathways and then use this origin information to provide catalyst principles that can enable the design of catalysts with enhanced radical rebound.

We examined the experimentally reported reaction between [(TQA\_Cl)Fe<sup>IV</sup>O]<sup>+</sup> and cyclohexane in acetonitrile,<sup>23</sup> which provides a key reaction that gives both rebound and dissociation pathways, experimentally and with direct dynamics trajectories. [(TQA\_Cl)Fe<sup>IV</sup>O]<sup>+</sup> is a high spin, S=2, complex that one might expect to observe dominant radical escape over rebound. Experimentally reported product yield data showed minor hydroxylation (15%) and major halogenation (78%).

Furthermore, addition of  $O_2$  resulted in complete suppression of the halogenation products, RCl and RBr, indicating the cage escape of the radical species as the dominant product pathway. However, it is unknown how the minor oxygenation product is formed. It could arise either from the rebound within the solvent cage before radical escape or from the reencounter of fully escaped radicals. As will be shown, our explicit solvent direct dynamics trajectories resolve this matter and show that fast rebounds are an inherent property of the HAT transition state and can occur in a dynamically concerted asynchronous manner. Our direct dynamics trajectories combined with machine learning analysis also revealed that the kinetic energy of the transferring hydrogen atom during the HAT reaction step controls rebound versus dissociation selectivity. We also established a connection between kinetic energy of the HAT hydrogen and the dynamical matching effect that triggers the opening of rebound product pathway. Manual manipulation of the hydrogen atom kinetic energy of the reaction provides the ability to control trajectory rebound versus dissociation. We used this physical origin to propose a general guideline for catalyst design that can be used to enhance (or diminish) the rebound pathway.

#### **COMPUTATAIONAL DETAILS**

All structure optimizations were performed using UB3LYP-D3(BJ)/def2-SVP level of theory in Gaussian 16 software package.<sup>24-28</sup> This method/basis set combination was shown to perform well for Fe-oxo spin state energies and barrier heights,<sup>29, 30</sup> and this method performed well in ours and Houk's trajectories to replicate the experimental chemoselectivity.<sup>17, 18</sup> For fully optimized structures, solvation effects were incorporated using the CPCM solvation model for acetonitrile.<sup>31, 32</sup> Frequency calculations and intrinsic reaction coordinate (IRC) analysis were used to confirm the transition-state structure connections.<sup>33</sup> Variational transition state optimizations using Polyrate-17 and Gaussrate-17B were used to determine the true nature of the optimized transition state structure.<sup>34, 35</sup> Natural charge calculations were performed using the NBO package implemented in Gaussian 16.<sup>36</sup>

Explicit solvent direct dynamics trajectory simulations were performed using our program Milo,<sup>37</sup> which uses multilayer ONIOM(QM/MM) method implemented in Gaussian 16 for the calculation of forces and energies.<sup>38</sup> UB3LYP(B3BJ)/def2-SVP level of theory was used to treat the solute (HAT transitions state) and custom OPLS force field for the solvents.<sup>39</sup> Packmol software was used to pack 200 acetonitrile solvents around the HAT transition state in a spherical manner with 33.0 Å diameter to maintain the solvent density.<sup>40</sup> Solvent molecules were then classically sampled and NVT equilibrated for 18 picoseconds (ps) using the Berendsen thermostat at the experimental

temperature of 233.15 K (see Supporting Information (SI) for more details).<sup>41</sup> Quasiclassical/classical (quasiclassical solute sampling/classical solvent sampling) direct dynamics trajectories were initialized from four different solvent configurations (12 ps, 14 ps, 16 ps, and 18 ps) using local mode and thermal sampling of the HAT transition state structure at the experimental temperature (233.15K), which includes zero-point energy. All NVE trajectories were then propagated with a 0.75 fs time step. We also executed implicit solvent quasiclassical trajectory simulations that used a similar procedure, and were also performed using our program Milo<sup>42</sup> that employed Gaussian 16 to calculate energies and forces at the UB3LYP-D3(BJ)/def2-SVP(cpcm=acetonitrile) level of theory.<sup>24-28, 31</sup>

For the machine learning analysis, a well-balanced hand-picked dataset was prepared consisting of 50 rebound and 50 intermediate/dissociation trajectories. Machine learning analysis of the dynamical trajectories used the following general input features: kinetic energies of the HAT hydrogen, Fe-oxo catalyst, and cyclohexane radical species, vibrational mode quanta, vibrational mode velocities, and vibrational mode energies. Training and testing were performed for 25 different machine learning classification algorithms implemented in the Scikit-learn Python library. The accuracy of every model was determined by a 10-fold cross validation. Hyperparameter optimization of the best machine learning models were performed using the Optuna automated hyperparameter optimization software framework. The SHapley Additive exPlanations (SHAP) algorithm was used to analyze the machine learning model feature importances. Further machine learning analysis details can be found in the SI.

### **RESULTS AND DISCUSSION**

#### **Static Transition State**

The [(TQA\_Cl)Fe<sup>IV</sup>O]<sup>+</sup> complex (Figure 2a, TQA = tris(quinolyl-2-methyl)amine) reported by Que is a synthetic mimic of a halogenase enzyme and provides a highly sensitive probe for the selectivity between radical pair rebound versus radical pair dissociation pathway products.<sup>23</sup> In its reaction with cyclohexane, halogenation is the major product (~78%) and this is typically interpreted as resulting from a radical pair dissociation pathway followed by a second halogen atom abstraction step. Cyclohexane hydroxylation is the minor product (~15%) that could occur either through fast radical pair rebound or through reencounter of the escaped radicals. We chose to analyze this C-H functionalization reaction with direct dynamics trajectories and machine learning because it gives a mixture of dissociation and rebound products. Prior DFT calculations of the reaction between

[(TQA\_Cl)Fe<sup>IV</sup>O]<sup>+</sup> and cyclohexane by Srnec showed that the HAT and post-HAT reactivity occurs exclusively through the quintet spin state, and the next lowest energy triplet spin state is as much as 9 kcal/mol higher in energy (Figure S1b).<sup>30</sup> Therefore, this reaction system is well suited for direct dynamics trajectories because dissociation and rebound pathways can be modeled using only the quintet spin state.

The DFT optimized HAT transition state between [(TQA\_Cl)FeIVO]+ and cyclohexane is shown in Figure 2b. For an Fe-oxo transition state, it has a moderately late (C-H = 1.24 Å) and tight (O-H = 1.30 Å) structure. The nearly linear C-H-O angle (168.9°) indicates that the HAT process occurs through the  $\sigma_{z^2}^*$  orbital of the iron-oxo moiety in the quintet spin state (Figure S1c, the  $\sigma$ -pathway). Since the  $\pi$ -pathway involves a triplet spin state, which is as much as 9 kcal/mol higher in energy, we have neglected spin crossover in the current trajectories. From the HAT transition-state structure, intrinsic reaction coordinate (IRC) calculations followed by geometry optimization identified the existence of an intermediate species on the potential-energy surface and is shown in Figure 2c. This static DFT optimized intermediate represents a radical-pair structure consisting of a fully formed Fe(OH) species (O-H = 0.99 Å) bound to the cyclohexane radical (C-H = 1.88 Å) though weak interaction (C···O = 2.87 Å). Previous analysis of this reaction with static DFT calculations showed a nearly barrierless process for radical pair dissociation and a barrier of about 1.4 kcal/mol for rebound (Figure S1b).<sup>30</sup>

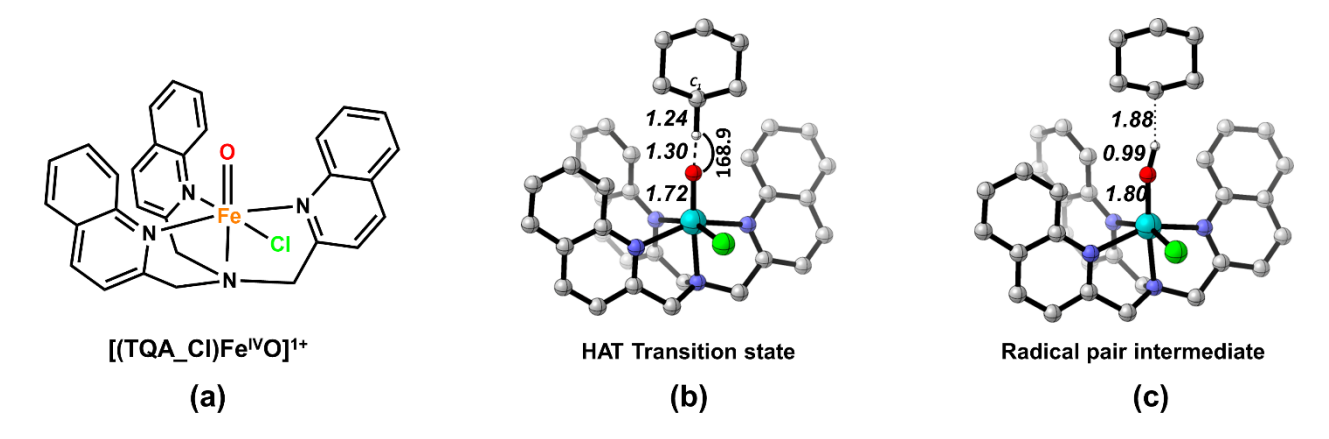


**Figure 2**. a) The  $[(TQA_Cl)Fe^{IV}O]^+$  complex. b) 3D rendering of the HAT transition state. c) The putative radical pair intermediate with key bond distances (Å) and angles (degree) calculated using UB3LYP-D3(BJ)/def2-SVP(cpcm, acetonitrile).

A small barrier for rebound and nearly barrierless dissociation could potentially explain the origin of the experimentally observed rebound ( $\sim$ 15%) versus dissociation ( $\sim$ 78%) selectivity. However, this statistical transition-state theory type of rationalization requires the existence of a

genuine radical-pair intermediate in the reaction mechanism. In some reactions, experiments point to radical pair intermediates with tens of picoseconds of lifetime, while in others there is no evidence for such a species. For example, hypersensitive radical probe/clock experiments of Newcomb on cyctochrome-P450 catalyzed hydroxylation reactions measured the lifetime of the putative radical pair intermediates in the range of 80 to 200 fs, which is too short a lifetime to be considered as a genuine, long-lived intermediate.<sup>12-14</sup> A combined experimental and static DFT study by Sarkar on methylcubane hydroxylation by cytochrome P450 implied the possible existence of a fast rebound processes and dynamic effects dictating the lifetime of the radical pair intermediate.<sup>15</sup> Based on a static transition-state reactive mode kinetic energy distribution model for synthetic heme and non-heme Fe-oxo complexes, Srnec has suggested that the HAT initiated rebound versus dissociation corresponds to a nonequilibrium ballistic process.<sup>30</sup> More recently our direct dynamics simulations,<sup>17</sup> and later trajectories by Houk,<sup>18</sup> have established that most of the rebound reactions are dynamically concerted with HAT transition state motion, albeit with some nonsynchronous/lagging motion.

All these studies have implied to various extents to the possibility that some of the radical pair intermediates can be nonstatistical with a lifetime that is too short for using standard assumptions of statistical rate theories, such as transition state theory (TST) or RRKM theory.<sup>46, 47</sup> At such short time scales, the excess energy accumulated in the reactive ensemble may not have time for thermal equilibration, leading to the formation of activated hot intermediates.<sup>48</sup> Thus, standard transition-state theory based models of competing reaction pathways with barrier height control likely does not provide physically correct modeling of pathway selectivity.<sup>49, 50</sup> It is now well established that such nonstatistical behavior when an intermediate does not have a long enough lifetime for intramolecular vibrational energy redistribution (IVR), and this often results in non-IRC pathways.<sup>19,20</sup> Therefore, if the radical-pair intermediate is nonstatistical and short-lived, then direct dynamics trajectories can be used to model the reaction selectivity.

## **Explicit Solvent Direct Dynamics Simulations**

To determine the dynamical origin of rebound versus dissociation selectivity, and to decipher the role of solvent on the radical-pair intermediate lifetime, we used direct dynamics trajectories to simulate the time resolved motion for the reaction between [(TQA\_Cl)Fe<sup>IV</sup>O]<sup>+</sup> and cyclohexane surrounded by an explicit solvent cage. 200 acetonitrile molecules were packed around the HAT transition-state structure in the form of a spherical solvent shell of 33.0 Å diameter. The solvent was equilibrated around the frozen HAT transition state for 18 ps using a custom OPLS force field at the

experimental temperature of 233.15 K (see SI and Figure S4 for more details). Shown in Figure 3a is the solvent equilibrated HAT transition state after 18 ps of simulation time. We then initialized 100 vibrationally sampled dynamical trajectories from four different solvent configurations (12 ps, 14 ps, 16 ps, and 18 ps) each consisting of 25 trajectories, which enabled well-balanced starting points for trajectories. Trajectory force and energy calculations were performed using the ONIOM (QM/MM) multilayer methodology, where [(TQA\_Cl)Fe<sup>IV</sup>O]<sup>+</sup> and cyclohexane were treated at the unrestricted UB3LYP-D3(BJ)/def2-SVP level, and acetonitrile solvents were treated using the custom OPLS force field. All reactive trajectories were propagated on the quintet spin state surface. Our static DFT calculations and test trajectories propagated using a mixture of the two lowest spin states (triplet and quintet) showed the absence of any spin state crossover after hydrogen atom transfer (Figure S3).

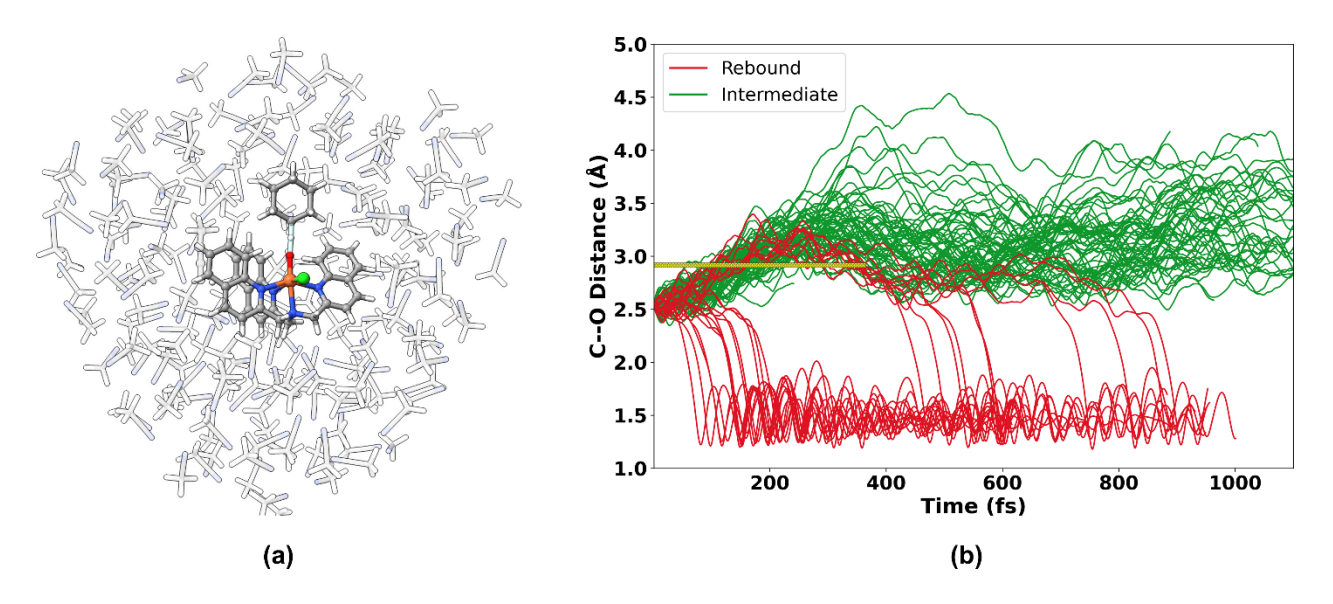


**Figure 3**. a) Solvent (200 acetonitrile) equilibrated (18 ps) HAT transition state for the reaction between  $[(TQA\_Cl)Fe^{IV}O]^+$  and cyclohexane (a few solvent molecules are removed for visual clarity). b) Plot of cyclohexane  $C_1$  to Fe-oxo oxygen distance (Å) verses simulation time (fs) for the forward direction trajectories in the presence of explicit acetonitrile solvent molecules. Red and green lines denote rebound and solvent caged radical-pair intermediate type trajectories respectively. The yellow bar represents the C-O distance in the DFT optimized radical-pair intermediate structure.

Out of 100 reactive trajectories, 10% of them recrossed and were not considered for the analysis. Figure 3b depicts the trajectory results where the cyclohexane  $C_1$  to Fe-oxo oxygen distance (in Å) is plotted versus simulation time (in femtoseconds (fs)). The initial hydrogen atom transfer from the C-H bond of cyclohexane to the Fe-oxo fragment occurred within less than 30 fs. After this short period of time, trajectories diverge into different product forming pathways. Red colored lines represent rebound trajectories, typified by shortening of the  $C_1$  to -OH distance, leading to the

formation of cyclohexanol. The remaining green colored lines represent the radical-pair intermediate type species encapsulated by the surrounding acetonitrile solvent molecules. These species represent the caged intermediates observed in several experimental studies, which likely take several ps to eventually undergo solvent cage escape (which is beyond the scope of the present study). Reencountering of such escaped radicals results in halogenated products. Based on our trajectory results, we anticipate 25% of the trajectories to rebound and 75% trajectories to eventually dissociate. This product distribution is in fair agreement with the experimental report by Que where minor product was rebound hydroxylation ( $\sim$ 15%) and major halogenated product was shown to originate from dissociation ( $\sim$ 78%).<sup>23</sup>

Interestingly, our trajectories showed two types of rebound (red lines), one that occurs within a very short timescale (115.5  $\pm$  30 fs, 57%), which is evidence for the potential existence of a nearly concerted, albeit nonsynchronous, rebound pathway,<sup>13, 51-53</sup> and another that occurs through a dynamically stepwise fashion with a reasonably longer radical-pair intermediate lifetime ( $\sim$ 508.5 $\pm$ 120 fs, 43%). This finding of both concerted and stepwise rebound processes is reminiscent of Goldberg's kinetic measurements of a corrole ligated Fe(OH) complex.<sup>54</sup> Our lifetime measurements are also in agreement with the dynamics simulations of cytochrome P450 enzyme models<sup>18, 55, 56</sup> and simulation of the radical oxygen rebound during oxidation of isobutane by dimethyldioxirane.<sup>57</sup>

The yellow bar in Figure 3b represents the DFT optimized radical-pair intermediate structure (C-O = 2.9 Å). A close examination of the trajectories showed that the late stepwise rebounds originate from the cage effect of the solvent, where radical-pair intermediates generated from the HAT transition state are shuttled back into the rebound pathway by the surrounding solvent. However, it is intriguing to note that the first type of ultrafast rebound trajectories never reached this radical-pair intermediate structure and occurs in a concerted, yet asynchronous, manner.<sup>17</sup> These trajectories essentially skipped the radical-pair intermediate type structure en route to the rebound product. Also very interesting, the solvent cage seems to have no significant influence on this type of rebound because it occurs at such a short time scale. This suggests that the first set of rebound trajectories is an inherent property of the HAT transition state and minimally influenced by solvent. As such, rebound should occur even in the gas phase trajectories.<sup>17, 18</sup> Taken together, these findings confirm the dynamical nature of the rebound processes and are consistent with the observations of Srnec,<sup>30</sup> Soler,<sup>48</sup> and Sarkar<sup>15</sup> that post-HAT rebound is indeed a dynamically controlled nonsynchronous

concerted process, and HAT transition state and the post-HAT reactivity are dynamically coupled.<sup>17,</sup>

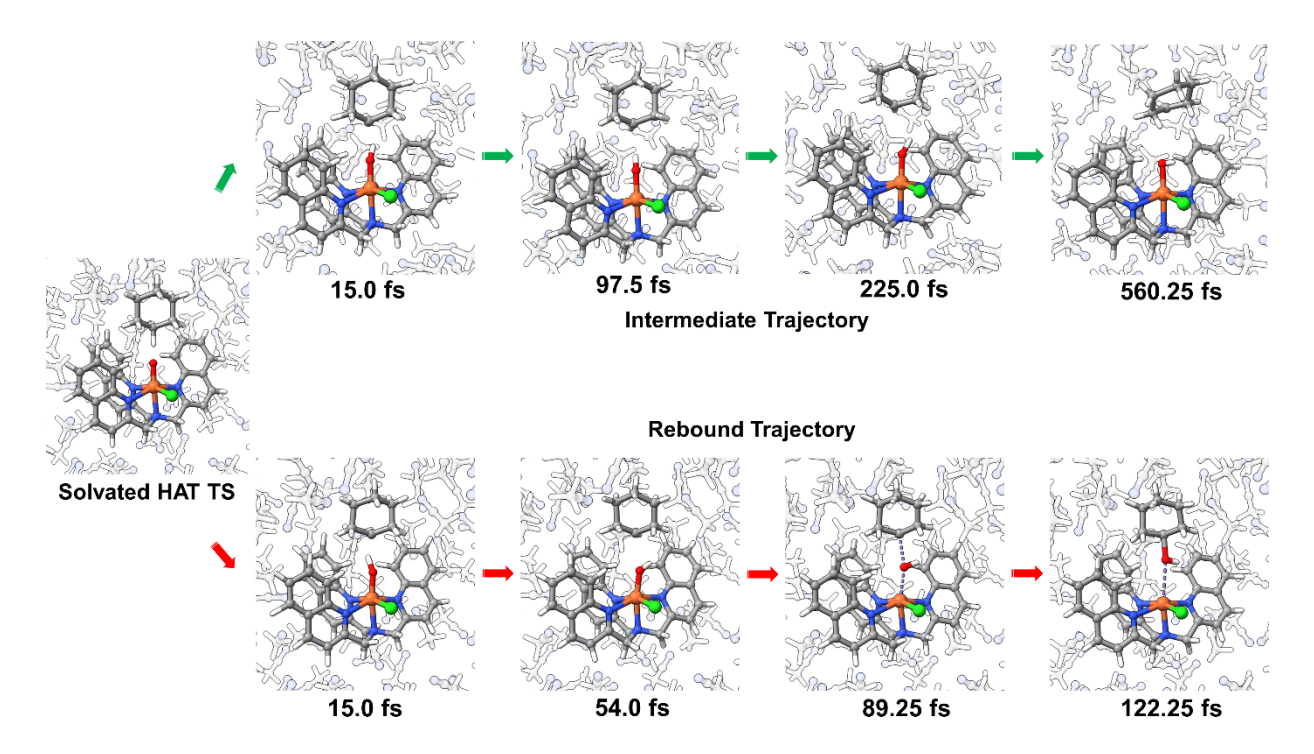


**Figure 4**. Snapshots of a typical rebound and caged radical-pair intermediate trajectory starting from acetonitrile solvated HAT transition state.

The dynamic coupling between HAT transition state and the rebound product pathway can be rationalized based on the concept of dynamic matching, originally proposed by Carpenter<sup>21, 22</sup> and popularized by Houk, Singleton, Doubleday, Hase, Tantillo, and others.<sup>58-60</sup> Dynamic matching implies a geometrical and dynamical correlation between entry of reactants into the transition state zone and their post-transition state exit.<sup>61</sup> Figure 4 depicts the evolution of a typical rebound and solvent caged radical-pair intermediate trajectory starting at the HAT transition state structure. After passing the HAT process, both trajectories evolve into a putative radical-pair type structure for a brief time. For the rebound trajectories, the hydroxyl group rotates along the Fe-oxo axis away from the cyclohexane radical to generate a direct carbon-oxygen contact before entering the rebound pathway, whereas for the intermediate type trajectories, the radical-pair undergoes steady elongation of the carbon to oxygen distance. This shows hydroxyl rotation is the preceding event leading to the rebound product channel whereas for the intermediate trajectories C-O bond elongation is the initial step, which is followed by hydroxyl rotation. Even when the hydroxyl group achieves the proper orientation for radical recombination at a later stage, rebound does not occur due to longer C-O distance which eventually leads to cage escape of the radical fragments. As such, hydroxyl group rotation is the

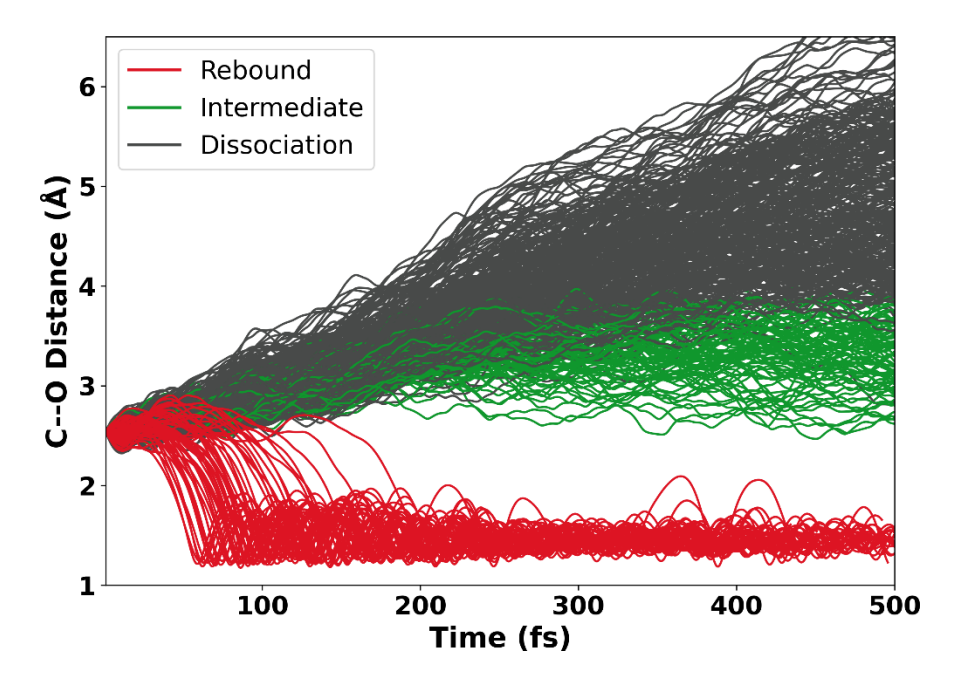
hallmark of rebound trajectories and energy transfer into the hydroxyl group rotational mode after HAT transition state is the key for dynamic matching. However, the underlying physical/chemical origin of this dynamic matching effect is unknown. Identifying from trajectory calculations the controlling physical feature of rebound versus dissociation selectivity is complex because each trajectory has a very complex set of initial conditions derived from sampling vibrational modes, and motion after the transition state involves decent along a highly complex multi-dimensional energy landscape. This prompted us to use machine learning to decode the complex set of transition-state conditions to identify the origin of dynamic reaction selectivity.

## **Machine Learning Analysis of Trajectories**

Because fast rebound is an inherent pathway that occurs from the HAT transition state and there is minimal influence from explicit interactions with solvent, we decided to use implicit solvent trajectory data for our machine learning analysis. This was an important decision because implicit solvent trajectories are significantly computationally less expensive and for machine learning there is the need to have a large dataset of trajectories. In order to generate enough data for machine learning, we performed 500 quasiclassical direct dynamics trajectories using unrestricted UB3LYP-D3(BJ)/def2-SVP level of theory in implicit solvation model for acetonitrile. All the reactive trajectories were propagated on the quintet spin state surface. Out of 500 reactive trajectories, 13% of them recrossed and were not considered in our later machine learning classification analysis.

Figure 5 depicts the result of our trajectories, where the cyclohexane  $C_1$  to Fe-oxo oxygen distance (in Å) is plotted versus simulation time (in fs). After the initial hydrogen atom transfer from the C-H bond of cyclohexane to the Fe-oxo fragment ( $\sim$ 30 fs), trajectories diverge into different product forming pathways. Red colored lines represent rebound trajectories, typified by shortening of the  $C_1$  to -OH distance, leading to the formation of cyclohexanol. The remaining trajectories were classified as dissociation (gray) or radical-pair intermediate (green) based on their relative  $C_1$  to -OH distance after 500 fs of trajectory time. Considering the DFT optimized transition state  $C_1$  to -OH distance of 2.54 Å, any trajectory with  $C_1$ -OH distance greater than 4.0 Å was considered as dissociation and all others were classified as radical-pair intermediate type. Our trajectories resulted in 13% ultrafast rebound and 87% radical-pair intermediate/dissociation types. Out of this 87%, a fraction of them could be pushed to rebound if solvent cage was present. In line with our explicit solvent simulations, these implicit solvent trajectories also retained the ultrafast nature of the

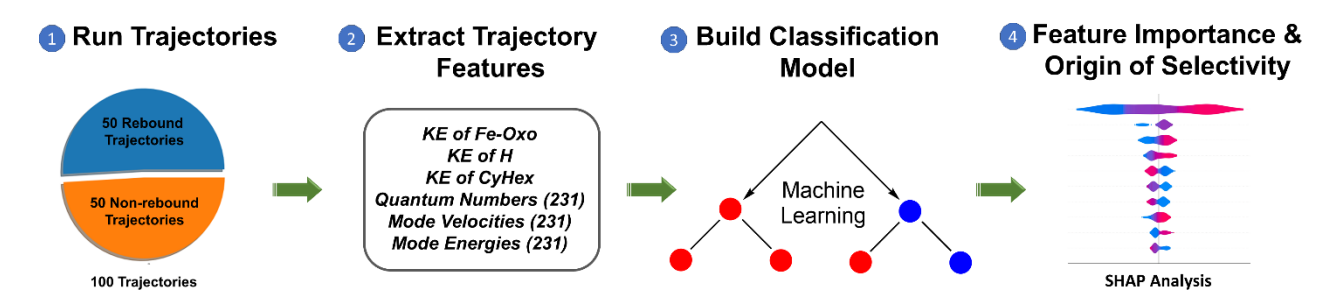
rebound. It is clear from these simulations that in the absence of an explicit solvent cage, dissociation trajectories quickly escape the radical-pair intermediate region of the potential energy surface.



**Figure 5**. Plot of cyclohexane  $C_1$  to Fe-oxo oxygen distance (Å) versus simulation time (fs) for the forward direction trajectories. Red, green, and gray colored lines respectively denote classification as rebound, radical-pair intermediate, and dissociation trajectories. Trajectory calculations were performed using UB3LYP-D3(BJ)/def2-SVP(cpcm=acetonitrile).

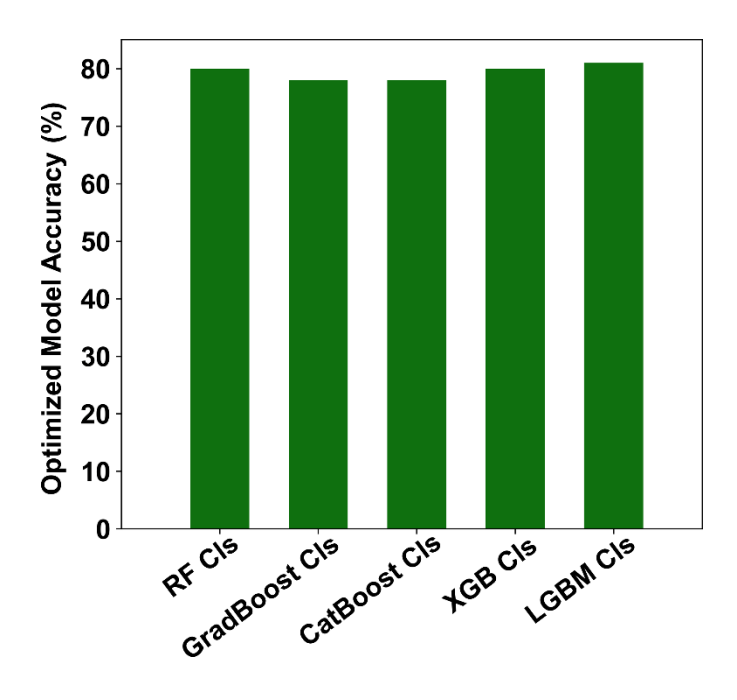
In our trajectories we used velocity-only sampling of the transition state, which we have previously shown to yield nearly identical results to sampling both velocities and geometries.<sup>62</sup> Within each trajectory there is zero-point vibrational energy, thermally excited vibrational energy, and directionality of each vibrational mode. Correlating the very subtle differences in each trajectory to the product outcome is extremely complex. To tackle this problem, we used machine learning classification models<sup>63</sup> capable of learning and differentiating which HAT trajectory features correlate with rebound versus non-rebound product forming pathways. Out of our 500 reactive trajectories, there were only 53 well-characterized rebound trajectories. Thus, in order to generate a well-balanced dataset of rebound versus non-rebound types, we manually analyzed each trajectory and handpicked 50 rebound and 50 non-rebound consisting of 25 intermediate and 25 dissociation trajectories. Throughout the following discussion non-rebound refers to intermediate/dissociation type trajectories. A schematic representation of our machine learning workflow is depicted in Figure 6. From the selected 100 trajectories, we extracted key features such as kinetic energies of the Fe-oxo species, cyclohexane radical fragment, and the hydrogen atom participating in the HAT process, as

well as the vibrational mode quanta, velocities, and energies for the first 30 vibrations. Similar to our previous approaches, we used the Scikit-Learn Python library to train and test different classification algorithms with a 10-fold cross validation to determine the accuracy of the model,<sup>62, 64, 65</sup> followed by feature importance analysis using the SHapley Additive exPlanations (SHAP) algorithm.<sup>45</sup>



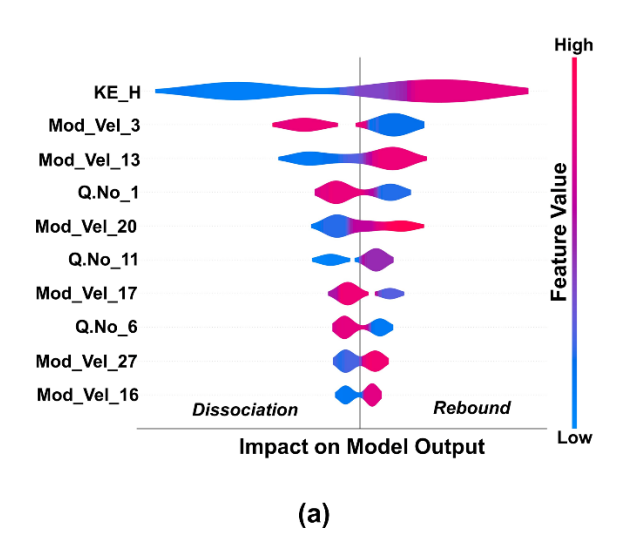
**Figure 6**. A schematic representation of our machine learning classification workflow. 50 rebound and 50 non-rebound trajectories with features including kinetic energy of the fragments, vibrational quanta, mode energies, and mode velocities were used as the basis of supervised classification machine learning analysis with feature importance extracted from SHAP analysis.

Supervised machine learning algorithms were used to analyze labeled trajectory data (rebound versus non-rebound) for training and testing on unlabeled testing data. We examined the performance of 25 supervised machine learning classification algorithms available in Scikit-Learn, which include linear models, ensemble models, tree-based models, support vector machines, nearest neighbors, calibration based, and discriminant analysis based.<sup>43</sup> A complete list of selected models and their mean accuracy can be found in the SI and Figure S5. It is interesting to note that classification models with baseline accuracy close to or more than 70% belong to ensemble, linear, or boost models (Figure S5). We then selected the best performing models with more than 75% accuracy (RandomForestClassifier, GradientBoostingClassifier, CatBoostClassifier, XGBoostClassifier, LightGBMClassifier) for hyperparameter optimization (see SI for details). Figure 7 shows the hyperparameter optimized five best performing models for rebound versus non-rebound classification problem. LGBMClassifier turned out to be our best performing model with classification accuracy of 81%. This is very solid accuracy given the difficulty of classifying trajectories that have only small differences in features (large feature space overlap) and fundamentally semi-chaotic nature of trajectories during propagation.<sup>62, 64</sup> Importantly, this accuracy is high enough to allow interrogation of the models for feature importance.



**Figure 7**. A plot of rebound versus non-rebound classification accuracy for the five best performing supervised machine learning models. RF Cls = RandomForestClassifier, GradBoost Cls = GradientBoostingClassifier, CatBoost Cls = CatBoostClassifier, XGB Cls = XGBoostClassifier, LGBM Cls = LightGBMClassifier.

We then extracted the most important features that influence the predictions made by the optimized LGBMClassifier model using the SHAP algorithm,<sup>45</sup> which gives information about the contribution of each feature value to the impact on the model output. The SHAP analysis shown in Figure 8a plots the 10 most important features on the y-axis in the order of their importance to the model output (rebound versus non-rebound) plotted in the x-axis. Red/blue color indicates high/low magnitude of the feature value (see Figure S6 for SHAP plots of other models). It is evident from Figure 8a that kinetic energy of the hydrogen atom participating in the HAT process (labeled as *KE\_H*) is the most important feature. A larger magnitude of *KE\_H* (red) prefers to rebound and a lower magnitude of *KE\_H* (blue) prefers dissociation as the major outcome. This finding is bolstered by Figure 8b where *KE\_H* value is plotted against rebound and non-rebound outcomes obtained from our dynamic trajectories. It is also interesting to note that other features, such as vibrational mode quanta and mode velocities, also play a role in dictating the trajectory outcome, although their impact on the model output is relatively low (Figure 8a).



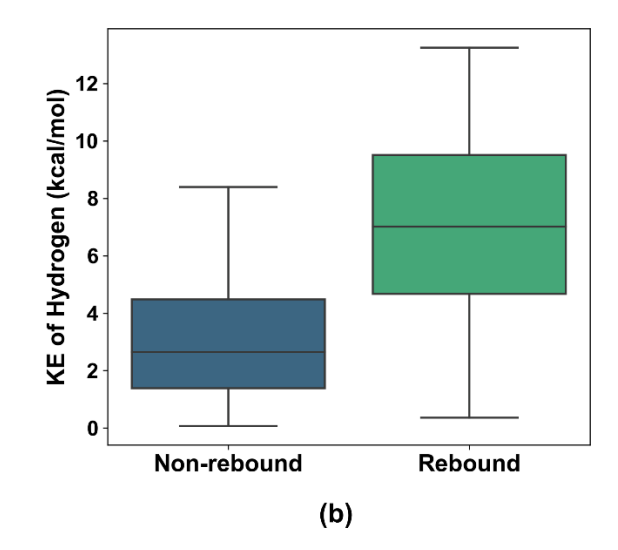


**Figure 8**. a) Feature importance plot from SHAP analysis showing that kinetic energy of the HAT hydrogen atom (*KE\_H*) is the most important feature that differentiates rebound versus non-rebound trajectories. Higher feature values are in red and lower feature values are in blue. b) Box plot of kinetic energy of the HAT hydrogen (in kcal/mol) for non-rebound and rebound trajectories.

We then decomposed the KE\_H feature into contributions from all the 231 individual normal modes of the HAT transition state (Figure S7). Kinetic energy contribution from the imaginary mode (normal mode 1) was found to be the most important contributor to KE\_H value, along with a few other higher modes (modes 101, 114, 123, 132, 136, 139, and 147). This suggests that the kinetic energy contribution from the reaction coordinate motion has the potential to control the trajectory outcomes. To test this hypothesis, we selected a well-defined dissociation trajectory and then manually altered the imaginary vibrational mode energy to add from 0.75 kcal/mol to 6.6 kcal/mol of additional energy (the original imaginary mode energy was 0.23 kcal/mol), which was done by controlling the quanta value at 2 cm<sup>-1</sup>. See the SI for details about how our Milo program treats sampling of the imaginary vibrational mode and how to control it. Importantly, most of the added energy is translated into kinetic energy of the HAT hydrogen atom (Figure S8). As illustrated in Figure 9a, lower quanta (300-700) maintained the dissociation outcome (gray lines), but as the quanta number crossed 800 units (>3.0 kcal/mol) the trajectory with an inherent preference for dissociation started to rebound (colored lines). It is interesting to note that as the magnitude of quanta increased from 800 to 1500 the time required for rebound decreased from  $\sim$ 135 fs to  $\sim$ 95 fs. This observation agrees with our conclusions from the machine learning analysis where higher magnitudes of the KE\_H feature leads to earlier rebound. With the discovery that the transferring hydrogen kinetic energy

feature is important we wondered how this energy fundamentally determines the outcome of most trajectories.

Figure 9b illustrates the dynamic matching concept that we previously described for this reaction (cf. Figure 4), where gray lines indicate non-rebound and colored lines indicate rebound trajectories as a function of C-O-H angle and C-O bond distance. Non-rebound trajectories showed an elongation in the C-O bond distance as the primary event whereas rebound trajectories showed C-O-H angle change (hydroxyl rotation) along the Fe-oxo axis followed by radical recombination (shortening of C-O distance). This indicates that the hydroxyl rotation motion is the key entry gate to the rebound pathway. Figure 8c plots the kinetic energy of the Fe-oxo oxygen atom for the first 140 fs of trajectory time, which shows nearly no change in the oxygen kinetic energy for the non-rebound trajectories (gray lines), whereas excess kinetic energy builds up in rebound trajectories (colored lines). It is interesting to note that for rebound trajectories the oxygen atom starts to accumulate kinetic energy very early just after the HAT process (40–60 fs), which means collision between oxygen and HAT hydrogen (with excess kinetic energy) transfers a part its energy to the oxygen to initiate the hydroxyl rotation. Thus, excess energy on the HAT hydrogen is the root cause of Fe(OH) bond rotation, and hence the origin of dynamic matching that opens up the rebound product pathway.

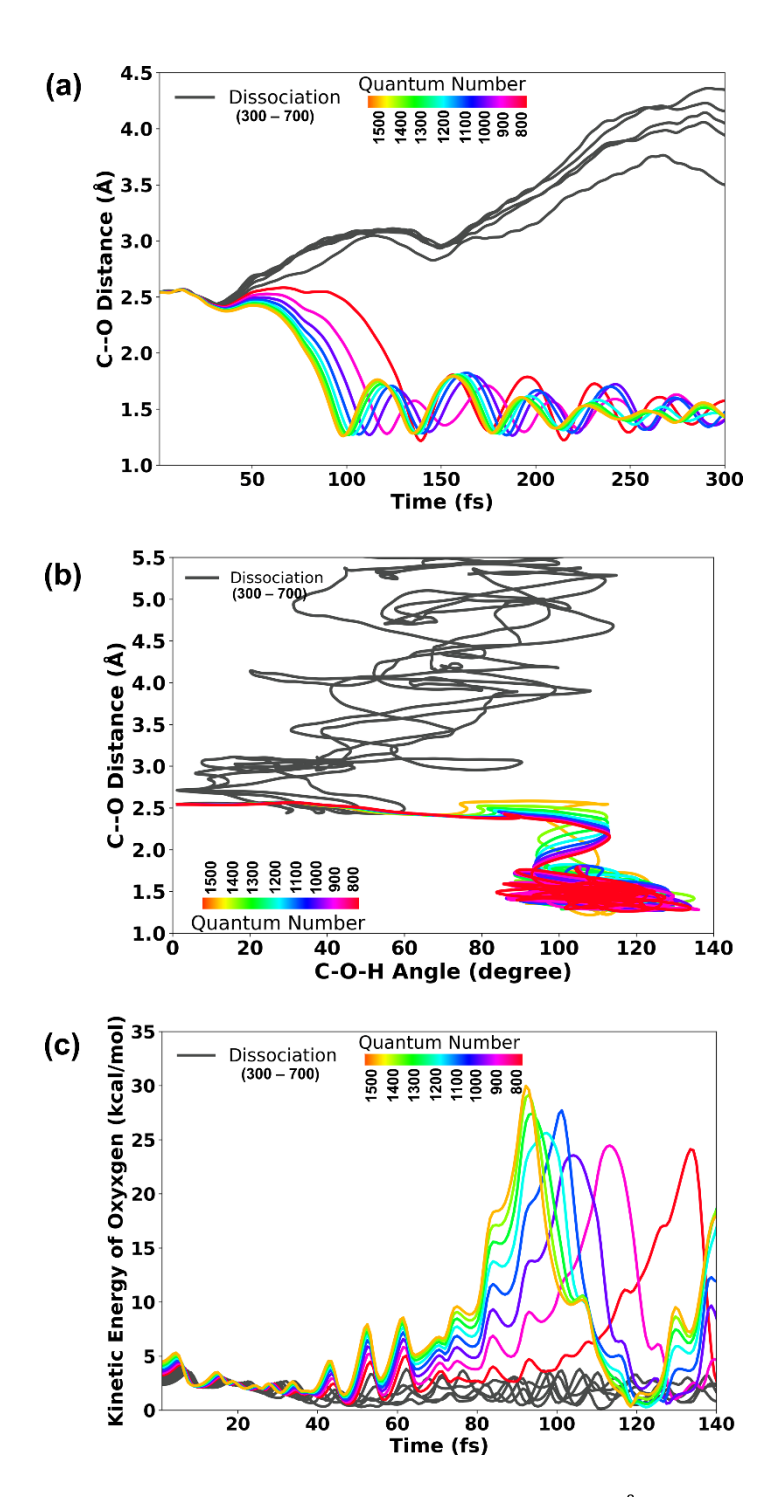


**Figure 9**. a) Plot of cyclohexane  $C_1$  to Fe-oxo oxygen distance (Å) verses simulation time (fs) illustrating the effect of imaginary mode quanta (300–1500) on the outcome of a typical dissociation trajectory. b) Plot illustrating the dynamical matching concept where the C-O-H angle (angle formed between the cyclohexane radical carbon and the newly formed O-H bond) is plotted versus the C---0 bond distance (in Å). c) Evolution of kinetic energy of the Fe-oxo oxygen (in kcal/mol) as a function of simulation time. Gray lines represent non-rebound and colored lines (based on quantum number) represent rebound trajectories.

### **Design Principles**

Although *KE\_H* is the most important feature in our machine learning models, experimental modulation of its magnitude to control the outcome of the HAT process is not obvious. Therefore, to enable catalyst design principles based on this fundamental physical feature, we decided to determine how the Fe-oxo catalyst can be chemically modified to alter this transition state feature and therefore control the post-HAT reaction selectivity.

We speculated that one strategy to increase the transferring hydrogen kinetic energy is to make the post HAT reactive surface more exothermic. The Bell-Evans-Polanyi principle<sup>66, 67</sup> and Hammond's postulate<sup>68</sup> provides a straightforward framework to envision this change by inducing an earlier and looser transition state (short C-H and long O···H bond distances) that could provide a more exothermic reactive surface<sup>16</sup> with more rebound compared to a later and tighter transition state with less rebound. Generally, early HAT transition states are typified by wider potential energy surface and lower magnitudes of imaginary frequency.<sup>69</sup> Which in turn indicates lower magnitudes of the imaginary mode force constant. The imaginary vibrational mode of the HAT transition state consists of the motions of the O···H···C moiety, where H is positively charged, and O and C are negatively charged. Shaik<sup>69</sup> previously established that a simple relationship for the force constant can be derived by considering the electrostatic potential (V) across the O<sup>δ.</sup>····H<sup>δ.</sup>····C<sup>δ.</sup> moiety as shown in eq. 1. Here, Q<sub>0</sub>, Q<sub>H</sub>, and Q<sub>C</sub> are charges, and R<sub>O·H</sub>, R<sub>C·H</sub>, and R<sub>C·O</sub> correspond to O·H, C·H, and C·O distances in the HAT transition state structure. The second derivative of V (eq. 2), with respect to the movement of the O, H, C atoms, will result in the force constant of the O<sup>δ.</sup>···H<sup>δ.</sup>···C<sup>δ.</sup> interaction. See reference 69 for more details of this derivation.

$$V = -\frac{|Q_O| * |Q_H|}{R_{O-H}} - \frac{|Q_C| * |Q_H|}{R_{C-H}} + \frac{|Q_O| * |Q_C|}{R_{C-O}}$$
(1)

$$\frac{d^2V}{dR^2} \approx k = -\frac{1}{2} \frac{|Q_O| * |Q_H|}{R_{O-H}^3} - \frac{1}{2} \frac{|Q_C| * |Q_H|}{R_{C-H}^3}$$
(2)

Equation 2 provides a straightforward way to control the force constant of the imaginary mode, and thereby the nature of the post-HAT potential energy surface. Thus, we reasoned that for a fixed substrate, such as cyclohexane ( $Q_C$  and  $Q_H$  are assumed to be constant), any modification in the iron-oxo catalyst that results in lowering the negative charge on the oxygen (more electrophilic) may lead to lower imaginary mode force constant, and thereby an earlier transition state, which in turn should result in more rebound. The opposite condition would result in more dissociation. This

reasoning is in agreement with the kinetic energy density (KED) analysis of Srnec et al., who showed HAT transition state with lower imaginary mode frequency may result in rebound product channel.<sup>30</sup> As such, judicial functionalization of the Fe-oxo complex to alter the electrostatics interaction at the  $O^{\delta_-} \cdots H^{\delta_+} \cdots C^{\delta_-}$  reaction coordinate motion could potentially control rebound versus dissociation selectivity.

As proof of principle, we considered the [(TQA Cl)Fe<sup>IV</sup>O]+ complex with hypothetical methoxy substituents (Figure 10a) and hypothetical cyano substituents (Figure 10b) on the TAQ ligand core. The methoxy functionalization makes the Fe-oxo oxygen more negatively charged ( $Q_0 = -0.70$  au) and cyano functionalization makes it less negatively charged ( $Q_0 = -0.60$  au) compared to the parent nonfunctionalized complex ( $Q_0 = -0.68$  au). As evident from Figure 10, methoxy functionalization made the transition state  $0\cdots H\cdots C$  interaction later (C-H = 1.25 Å) and tighter ( $C\cdots O$  = 2.54 Å) whereas the cyano functionalization resulted in an earlier (C-H = 1.20 Å) and looser (C···O = 2.61 Å) structure. The methoxy functionalized complex possesses a substantially higher imaginary frequency (-1073.8 cm 1) as compared to that of cyano-functionalized complex (-713.5 cm<sup>-1</sup>). All these features make the methoxy complex less exothermic and cyano complex more exothermic as evident from the IRC plot in Figure 10. This suggests non-rebound for methoxy-substituted reaction and rebound for the cyanosubstituted reaction as the major product channel. Indeed, our trajectories substantiated this logic and prediction, which are illustrated at the right end of Figure 10. Methoxy functionalization yielded only 8% of rebound products whereas cyano functionalization increased rebound to 42% compared to the 13% in the original non-functionalized [(TQA\_Cl)Fe<sup>IV</sup>O]+ complex. Overall, this indicates that simple chemical alternation generating an earlier transition-state structure will result in more rebound.

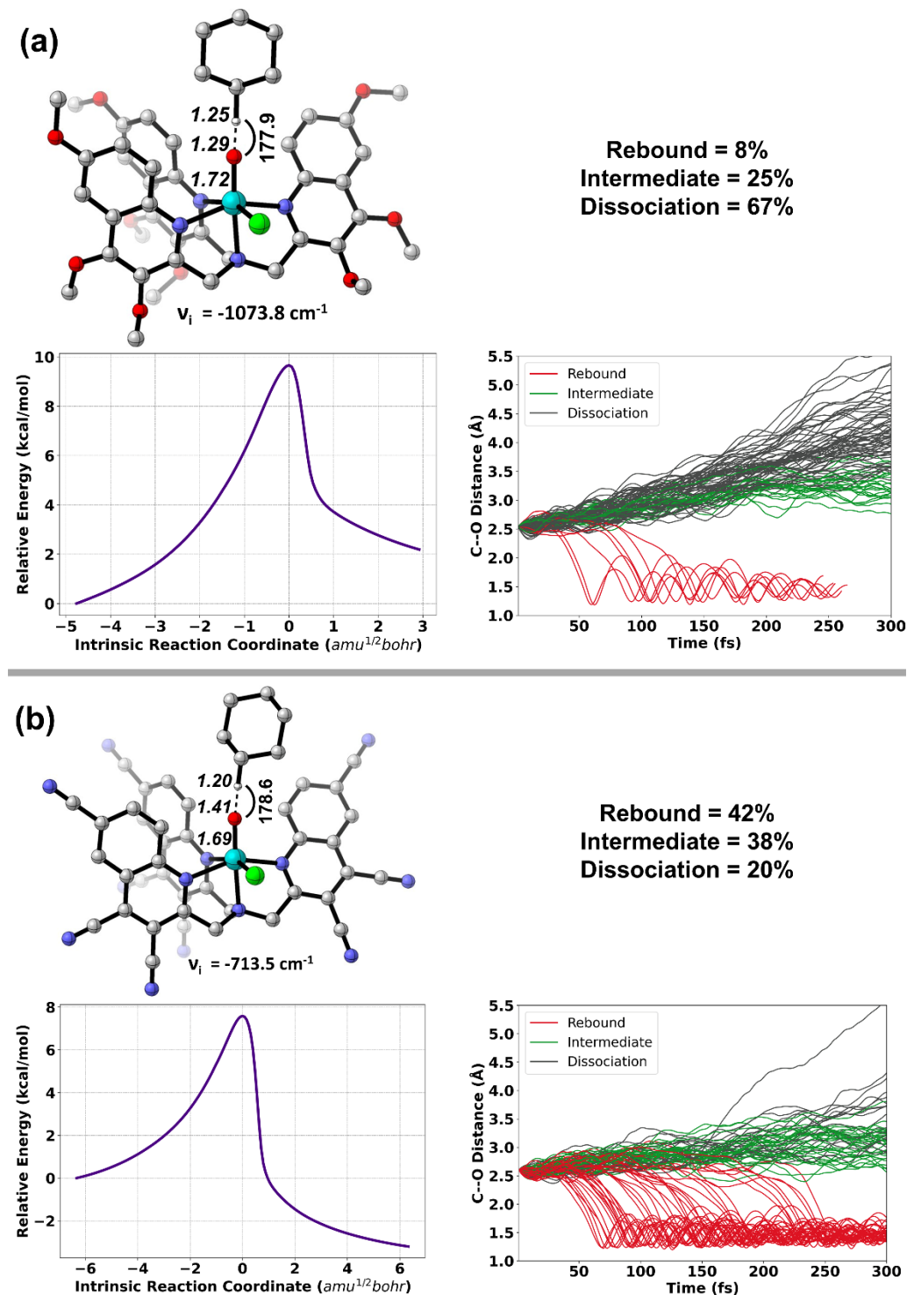


**Figure 10**. Effect of TQA ligand functionalization on the rebound versus non-rebound dynamic pathway selectivity. a) Optimized HAT transition-state structure of the methoxy functionalized [(TQA\_Cl)Fe<sup>IV</sup>O]<sup>+</sup> complex, its IRC pathway, and the corresponding quasiclassical direct dynamics trajectory results. b) Optimized HAT transition-state structure of cyano functionalized [(TQA\_Cl)Fe<sup>IV</sup>O]<sup>+</sup> complex, its IRC pathway, and the corresponding quasiclassical direct dynamics trajecotry results.

A reexamination of the transition state features of an experimentally known exclusive hydroxylation catalyst,  $[(PyNMe_3)Fe^vO(OAc)]^{2+,70}$  exhibited an even earlier (C-H = 1.18 Å) and looser (C···O = 2.65 Å) transition state compared to the cyano functionalized  $[(TQA\_Cl)Fe^{Iv}O]^+$  complex (Figure S9a). Moreover, a much lower magnitude of the imaginary frequency (-674.90 cm<sup>-1</sup>) further confirms that this complex would show higher preference for rebound product. In line with this, our calculations confirmed that 92% of the trajectories resulted in the rebound product (Figure S9b). This observation buttresses our argument that an Fe-oxo complex possessing an early HAT transition state with shallow and wide HAT potential energy landscape having a more electrophilic oxygen may be an ideal candidate for an efficient rebound catalyst. <sup>16,71</sup> Furthermore, Fe-oxo complexes with non-rebound preference have a narrow energy surface that are likely to exhibit higher tunneling effect and large experimentally measured kinetic isotope effect (KIE) values, corroborating with experimentally reported KIE data collected by Srnec et al. <sup>30</sup>

### **CONCLUSION**

Explicit solvent (200 acetonitrile) direct dynamics trajectories were executed for the HAT reaction between [(TQA\_CI)Fe<sup>IV</sup>O]<sup>+</sup> and cyclohexane, and the ratio of rebound versus dissociation trajectories were consistent with experiment. These trajectories established the concerted, yet asynchronous, nature of the rebound process, and the potential existence of caged radical-pair intermediates in the post-HAT reactive surface of Fe-oxo complexes. 500 implicit solvent quasiclassical trajectories provided a dataset for an in-depth machine learning analysis of the transition-state physical/chemical factors that control rebound versus dissociation selectivity. This analysis revealed that the transferring hydrogen atom kinetic energy is the most important factor controlling selectivity, with a larger kinetic energy favoring rebound. This provides an explanation for our previously proposed dynamic matching effect in fast rebound trajectories that bypass the radical pair intermediate. We confirmed this physical origin by manually controlling the transferring hydrogen atom kinetic energy by modulating the reaction coordinate energy. This led to the general idea that catalysts can be tuned to increase radical pair rebound if the transition state has an earlier and looser geometry and corresponds to a more exothermic reaction profile.

SUPPORTING INFORMATION

Computational methods, free energy profiles, electron-shift diagram, variational transition states,

mixed spin trajectory calculations, details of explicit solvent trajectories, details of machine learning

analysis, decomposition of the KE H feature, dynamical trajectories of [(PyNMe<sub>3</sub>)Fe<sup>v</sup>O(OAc)]<sup>2+</sup>

complex, and xyz coordinates.

**NOTES** 

The authors declare no competing financial interest.

**ACKNOWLEDGEMENTS** 

We thank Brigham Young University and the Fulton Supercomputing Lab for computational

resources. We thank Dr. Justin K. Kirkland for the helpful discussions about machine learning. This

work was supported by the US National Science Foundation with award CHE-2244799.

**ORCID ID** 

Jyothish Joy: 0000-0002-2260-4329

Anthony J. Schaefer: 0009-0001-1735-6543

Matthew S. Teynor: 0000-0002-6981-4809

Daniel H. Ess: 0000-0001-5689-9762

CORRESPONDING AUTHOR

\*dhe@chem.byu.edu

**REFERENCES** 

(1) Ortiz de Montellano, P. R. Hydrocarbon Hydroxylation by Cytochrome P450 Enzymes. Chem. Rev. 2010,

110, 932-948

22

- (2) Groves, J. T.; McClusky, G. A. Aliphatic hydroxylation via oxygen rebound. Oxygen transfer catalyzed by iron. *J. Am. Chem. Soc.* **1976**, *98*, 859-861
- (3) Kovaleva, E. G.; Lipscomb, J. D. Versatility of biological non-heme Fe(II) centers in oxygen activation reactions. *Nat. Chem. Biol.* **2008**, *4*, 186-193
- (4) Cho, K.-B.; Hirao, H.; Shaik, S.; Nam, W. To rebound or dissociate? This is the mechanistic question in C– H hydroxylation by heme and nonheme metal—oxo complexes. *Chem. Soc. Rev.* **2016**, *45*, 1197-1210
- (5) Grant, J. L.; Mitchell, M. E.; Makris, T. M. Catalytic strategy for carbon–carbon bond scission by the cytochrome P450 OleT. *Proc. Natl. Acad. Sci. U. S. A.* **2016**, *113*, 10049-10054
- (6) Rettie, A. E.; Rettenmeier, A. W.; Howald, W. N.; Baillie, T. A. Cytochrome P-450—Catalyzed Formation of  $\Delta^4$ -VPA, a Toxic Metabolite of Valproic Acid. *Science* **1987**, *235*, 890-893
- (7) Drummond, M. J.; Ford, C. L.; Gray, D. L.; Popescu, C. V.; Fout, A. R. Radical Rebound Hydroxylation Versus H-Atom Transfer in Non-Heme Iron(III)-Hydroxo Complexes: Reactivity and Structural Differentiation. *J. Am. Chem. Soc.* **2019**, *141*, 6639-6650
- (8) Shaik, S.; Cohen, S.; Wang, Y.; Chen, H.; Kumar, D.; Thiel, W. P450 Enzymes: Their Structure, Reactivity, and Selectivity—Modeled by QM/MM Calculations. *Chem. Rev.* **2010**, *110*, 949-1017
- (9) Huang, X.; Groves, J. T. Beyond ferryl-mediated hydroxylation: 40 years of the rebound mechanism and C–H activation. *J. Biol. Inorg. Chem.* **2017**, *22*, 185-207
- (10) Groves, J. T.; Adhyam, D. V. Hydroxylation by cytochrome P-450 and metalloporphyrin models. Evidence for allylic rearrangement. *J. Am. Chem. Soc.* **1984**, *106*, 2177-2181
- (11) Shaik, S.; Cohen, S.; de Visser, Samuël P.; Sharma, Pankaz K.; Kumar, D.; Kozuch, S.; Ogliaro, F.; Danovich, D. The "Rebound Controversy": An Overview and Theoretical Modeling of the Rebound Step in C–H Hydroxylation by Cytochrome P450. *Eur. J. Inorg. Chem.* **2004**, 2004, 207-226
- (12) Newcomb, M.; Shen, R.; Choi, S.-Y.; Toy, P. H.; Hollenberg, P. F.; Vaz, A. D. N.; Coon, M. J. Cytochrome P450-Catalyzed Hydroxylation of Mechanistic Probes that Distinguish between Radicals and Cations. Evidence for Cationic but Not for Radical Intermediates. *J. Am. Chem. Soc.* **2000**, *122*, 2677-2686
- (13) Newcomb, M.; Le Tadic-Biadatti, M.-H.; Chestney, D. L.; Roberts, E. S.; Hollenberg, P. F. A nonsynchronous concerted mechanism for cytochrome P-450 catalyzed hydroxylation. *J. Am. Chem. Soc.* **1995**, *117*, 12085-12091
- (14) Toy, P. H.; Newcomb, M.; Hollenberg, P. F. Hypersensitive Mechanistic Probe Studies of Cytochrome P450-Catalyzed Hydroxylation Reactions. Implications for the Cationic Pathway. *J. Am. Chem. Soc.* **1998**, 120, 7719-7729
- (15) Sarkar, M. R.; Houston, S. D.; Savage, G. P.; Williams, C. M.; Krenske, E. H.; Bell, S. G.; De Voss, J. J. Rearrangement-Free Hydroxylation of Methylcubanes by a Cytochrome P450: The Case for Dynamical Coupling of C–H Abstraction and Rebound. *J. Am. Chem. Soc.* **2019**, *141*, 19688-19699
- (16) Pangia, T. M.; Yadav, V.; Gérard, E. F.; Lin, Y.-T.; de Visser, S. P.; Jameson, G. N. L.; Goldberg, D. P. Mechanistic Investigation of Oxygen Rebound in a Mononuclear Nonheme Iron Complex. *Inorg. Chem.* **2019**, *58*, 9557-9561
- (17) Joy, J.; Ess, D. H. Direct Dynamics Trajectories Demonstrate Dynamic Matching and Nonstatistical Radical Pair Intermediates during Fe-Oxo-Mediated C-H Functionalization Reactions. *J Am Chem Soc* **2023**, *145*, 7628-7637
- (18) Zhang, Y.; Cao, C.; She, Y.; Yang, Y.-F.; Houk, K. N. Molecular Dynamics of Iron Porphyrin-Catalyzed C— H Hydroxylation of Ethylbenzene. *J. Am. Chem. Soc.* **2023**, *145*, 14446-14455
- (19) Ess, D. H. Quasiclassical Direct Dynamics Trajectory Simulations of Organometallic Reactions. *Acc. Chem. Res.* **2021**, *54*, 4410-4422
- (20) Ma, X.; Hase, W. L. Perspective: chemical dynamics simulations of non-statistical reaction dynamics. *Philos. Trans. R. Soc. A* **2017**, *375*, 20160204
- (21) Carpenter, B. K. Dynamic Matching: The Cause of Inversion of Configuration in the [1,3] Sigmatropic Migration? *J. Am. Chem. Soc.* **1995**, *117*, 6336-6344

- (22) Carpenter, B. K. Nonstatistical Dynamics in Thermal Reactions of Polyatomic Molecules. *Annu. Rev. Phys. Chem.* **2004**, *56*, 57-89
- (23) Puri, M.; Biswas, A. N.; Fan, R.; Guo, Y.; Que, L. Modeling Non-Heme Iron Halogenases: High-Spin Oxoiron(IV)—Halide Complexes That Halogenate C—H Bonds. *J. Am. Chem. Soc.* **2016**, *138*, 2484-2487
- (24) Frisch, M. J.; Trucks, G. W.; Schlegel, H. B.; Scuseria, G. E.; Robb, M. A.; Cheeseman, J. R.; Scalmani, G.; Barone, V.; Petersson, G. A.; Nakatsuji, H.; Li, X.; Caricato, M.; Marenich, A. V.; Bloino, J.; Janesko, B. G.; Gomperts, R.; Mennucci, B.; Hratchian, H. P.; Ortiz, J. V.; Izmaylov, A. F.; Sonnenberg, J. L.; Williams-Young, D.; Ding, F.; Lipparini, F.; Egidi, F.; Goings, J.; Peng, B.; Petrone, A.; Henderson, T.; Ranasinghe, D.; Zakrzewski, V. G.; Gao, J.; Rega, N.; Zheng, G.; Liang, W.; Hada, M.; Ehara, M.; Toyota, K.; Fukuda, R.; Hasegawa, J.; Ishida, M.; Nakajima, T.; Honda, Y.; Kitao, O.; Nakai, H.; Vreven, T.; Throssell, K.; Montgomery, J. A., Jr.; Peralta, J. E.; Ogliaro, F.; Bearpark, M. J.; Heyd, J. J.; Brothers, E. N.; Kudin, K. N.; Staroverov, V. N.; Keith, T. A.; Kobayashi, R.; Normand, J.; Raghavachari, K.; Rendell, A. P.; Burant, J. C.; Iyengar, S. S.; Tomasi, J.; Cossi, M.; Millam, J. M.; Klene, M.; Adamo, C.; Cammi, R.; Ochterski, J. W.; Martin, R. L.; Morokuma, K.; Farkas, O.; Foresman, J. B.; Fox, D. J. Gaussian 16, Revision B.01; Gaussian Inc., Wallingford CT, 2016.
- (25) Becke, A. D. Density-functional thermochemistry. III. The role of exact exchange. *J. Chem. Phys.* **1993**, *98*, 5648-5652
- (26) Lee, C.; Yang, W.; Parr, R. G. Development of the Colle-Salvetti correlation-energy formula into a functional of the electron density. *Phys. Rev. B.* **1988**, *37*, 785-789
- (27) Grimme, S.; Ehrlich, S.; Goerigk, L. Effect of the damping function in dispersion corrected density functional theory. *J. Comput. Chem.* **2011**, *32*, 1456-1465
- (28) Weigend, F.; Ahlrichs, R. Balanced basis sets of split valence, triple zeta valence and quadruple zeta valence quality for H to Rn: Design and assessment of accuracy. *Phys. Chem. Chem. Phys.* **2005**, *7*, 3297-3305
- (29) Altun, A.; Breidung, J.; Neese, F.; Thiel, W. Correlated Ab Initio and Density Functional Studies on H<sub>2</sub> Activation by FeO<sup>+</sup>. *J. Chem. Theory Comput.* **2014**, *10*, 3807-3820
- (30) Maldonado-Domínguez, M.; Srnec, M. Understanding and Predicting Post H-Atom Abstraction Selectivity through Reactive Mode Composition Factor Analysis. *J. Am. Chem. Soc.* **2020**, *142*, 3947-3958
- (31) Cossi, M.; Rega, N.; Scalmani, G.; Barone, V. Energies, structures, and electronic properties of molecules in solution with the C-PCM solvation model. *J. Comput. Chem.* **2003**, *24*, 669-681
- (32) Postils, V.; Company, A.; Solà, M.; Costas, M.; Luis, J. M. Computational Insight into the Mechanism of Alkane Hydroxylation by Non-heme Fe(PyTACN) Iron Complexes. Effects of the Substrate and Solvent. *Inorg. Chem.* **2015**, *54*, 8223-8236
- (33) Fukui, K. The path of chemical reactions the IRC approach. Acc. Chem. Res. 1981, 14, 363-368
- (34) Zheng, J. B., J. L.; Meana-Pañeda, R.; Zhang, S.; Lynch, B. J.; Corchado, J. C.; Chuang, Y.-Y.; Fast, P. L.; Hu, W.-P.; Liu, Y.-P.; Lynch, G. C.; Nguyen, K. A.; Jackels, C. F.; Fernandez-Ramos, A.; Ellingson, B. A.; Melissas, V. S.; Villà, J.; Rossi, I.; Coitiño, E. L.; Pu, J.; Albu, T. V.; Ratkiewicz, A.; Steckler, R.; Garrett, B. C.; Isaacson, A. D.; Truhlar, D. G. Polyrate—version 2017; University of Minnesota, Minneapolis, MN, 2018.,
- (35) Zheng, J. B., J. L.; Zhang, S.; Corchado, J. C.; Meana-Pañeda, R.; Chuang, Y.-Y.; Coitiño, E. L.; Ellingson, B. A.; Truhlar, D. G. . Gaussrate 17, University of Minnesota, Minneapolis, MN, 2017.,
- (36) Reed, A. E.; Weinstock, R. B.; Weinhold, F. Natural population analysis. *J. Chem. Phys.* **1985**, *83*, 735-746
- (37) Schaefer, A. J.; Teynor, M. S.; Wohlgemuth, N.; Carlson, L.; Huang, J.; Pugh, S. L.; Grant, B. O.; Hamilton, R. S.; Carlsen, R.; Ess, D. H. *Milo, Revision 1.2*; Brigham Young University, Provo UT, 2023.
- (38) Dapprich, S.; Komáromi, I.; Byun, K. S.; Morokuma, K.; Frisch, M. J. A new ONIOM implementation in Gaussian98. Part I. The calculation of energies, gradients, vibrational frequencies and electric field derivatives1Dedicated to Professor Keiji Morokuma in celebration of his 65th birthday.1. *J. Mol. Struc-THEOCHEM* **1999**, *461-462*, 1-21

- (39) Jorgensen, W. L.; Maxwell, D. S.; Tirado-Rives, J. Development and Testing of the OPLS All-Atom Force Field on Conformational Energetics and Properties of Organic Liquids. *J. Am. Chem. Soc.* **1996**, *118*, 11225-11236
- (40) Martínez, L.; Andrade, R.; Birgin, E. G.; Martínez, J. M. PACKMOL: A package for building initial configurations for molecular dynamics simulations. *J. Comput. Chem.* **2009**, *30*, 2157-2164
- (41) Berendsen, H. J. C.; Postma, J. P. M.; van Gunsteren, W. F.; DiNola, A.; Haak, J. R. Molecular dynamics with coupling to an external bath. *J. Chem. Phys.* **1984**, *81*, 3684-3690
- (42) Teynor, M. S.; Wohlgemuth, N.; Carlson, L.; Huang, J.; Pugh, S. L.; Grant, B. O.; Hamilton, R. S.; Carlsen, R.; Ess, D. H. *Milo, Revision 1.1.0*; Brigham Young University, Provo UT, 2022.
- (43) Pedregosa, F.; Varoquaux, G.; Gramfort, A.; Michel, V.; Thirion, B.; Grisel, O.; Blondel, M.; Prettenhofer, P.; Weiss, R.; Dubourg, V.; Vanderplas, J.; Passos, A.; Cournapeau, D.; Brucher, M.; Perrot, M.; Duchesnay, É. Scikit-learn: Machine Learning in Python. *J. Mach. Learn. Res.* **2011**, *12*, 2825–2830
- (44) Akiba, T.; Sano, S.; Yanase, T.; Ohta, T.; Koyama, M. Optuna: A Next-generation Hyperparameter Optimization Framework. In Proceedings of the 25th ACM SIGKDD International Conference on Knowledge Discovery & Data Mining, Anchorage, AK, USA; 2019.
- (45) Lundberg, S. M.; Lee, S.-I. A unified approach to interpreting model predictions. In Proceedings of the 31st International Conference on Neural Information Processing Systems, Long Beach, California, USA; 2017.
- (46) Eyring, H. The Activated Complex in Chemical Reactions. J. Chem. Phys. 1935, 3, 107-115
- (47) Truhlar, D. G.; Garrett, B. C.; Klippenstein, S. J. Current Status of Transition-State Theory. *J. Phys. Chem.* **1996**, *100*, 12771-12800
- (48) Soler, J.; Gergel, S.; Klaus, C.; Hammer, S. C.; Garcia-Borràs, M. Enzymatic Control over Reactive Intermediates Enables Direct Oxidation of Alkenes to Carbonyls by a P450 Iron-Oxo Species. *J. Am. Chem. Soc.* **2022**, *144*, 15954-15968
- (49) Carpenter, B. K. Energy Disposition in Reactive Intermediates. Chem. Rev. 2013, 113, 7265-7286
- (50) Sun, L.; Song, K.; Hase, W. L. A S<sub>N</sub>2 Reaction That Avoids Its Deep Potential Energy Minimum. *Science* **2002**, *296*, 875-878
- (51) Black, K.; Liu, P.; Xu, L.; Doubleday, C.; Houk, K. N. Dynamics, transition states, and timing of bond formation in Diels—Alder reactions. *Proc. Natl. Acad. Sci. U. S. A.* **2012**, *109*, 12860-12865
- (52) Yang, Z.; Houk, K. N. The Dynamics of Chemical Reactions: Atomistic Visualizations of Organic Reactions, and Homage to van 't Hoff. *Chem. Eur. J.* **2018**, *24*, 3916-3924
- (53) Horn, B. A.; Herek, J. L.; Zewail, A. H. Retro-Diels–Alder Femtosecond Reaction Dynamics. *J. Am. Chem. Soc.* **1996**, *118*, 8755-8756
- (54) Zaragoza, J. P. T.; Yosca, T. H.; Siegler, M. A.; Moënne-Loccoz, P.; Green, M. T.; Goldberg, D. P. Direct Observation of Oxygen Rebound with an Iron-Hydroxide Complex. *J. Am. Chem. Soc.* **2017**, *139*, 13640-13643
- (55) Yoshizawa, K.; Kamachi, T.; Shiota, Y. A Theoretical Study of the Dynamic Behavior of Alkane Hydroxylation by a Compound I Model of Cytochrome P450. *J. Am. Chem. Soc.* **2001**, *123*, 9806-9816
- (56) Elenewski, J. E.; Hackett, J. C. Ab initio dynamics of the cytochrome P450 hydroxylation reaction. *J. Chem. Phys.* **2015**, *142*, 064307
- (57) Yang, Z.; Yu, P.; Houk, K. N. Molecular Dynamics of Dimethyldioxirane C–H Oxidation. *J. Am. Chem. Soc.* **2016**, *138*, 4237-4242
- (58) Doubleday, C.; Suhrada, C. P.; Houk, K. N. Dynamics of the Degenerate Rearrangement of Bicyclo[3.1.0]hex-2-ene. *J. Am. Chem. Soc.* **2006**, *128*, 90-94
- (59) Ussing, B. R.; Hang, C.; Singleton, D. A. Dynamic Effects on the Periselectivity, Rate, Isotope Effects, and Mechanism of Cycloadditions of Ketenes with Cyclopentadiene. *J. Am. Chem. Soc.* **2006**, *128*, 7594-7607

- (60) Lourderaj, U.; Hase, W. L. Theoretical and Computational Studies of Non-RRKM Unimolecular Dynamics. *J. Phys. Chem. A* **2009**, *113*, 2236-2253
- (61) Collins, P.; Kramer, Z. C.; Carpenter, B. K.; Ezra, G. S.; Wiggins, S. Nonstatistical dynamics on the caldera. *J. Chem. Phys.* **2014**, *141*, 034111
- (62) Rollins, N.; Pugh, S. L.; Maley, S. M.; Grant, B. O.; Hamilton, R. S.; Teynor, M. S.; Carlsen, R.; Jenkins, J. R.; Ess, D. H. Machine Learning Analysis of Direct Dynamics Trajectory Outcomes for Thermal Deazetization of 2,3-Diazabicyclo[2.2.1]hept-2-ene. *J. Phys. Chem. A* **2020**, *124*, 4813-4826
- (63) Keith, J. A.; Vassilev-Galindo, V.; Cheng, B.; Chmiela, S.; Gastegger, M.; Müller, K.-R.; Tkatchenko, A. Combining Machine Learning and Computational Chemistry for Predictive Insights Into Chemical Systems. *Chem. Rev.* **2021**, *121*, 9816-9872
- (64) Maley, S. M.; Melville, J.; Yu, S.; Teynor, M. S.; Carlsen, R.; Hargis, C.; Hamilton, R. S.; Grant, B. O.; Ess, D. H. Machine learning classification of disrotatory IRC and conrotatory non-IRC trajectory motion for cyclopropyl radical ring opening. *Phys. Chem. Chem. Phys.* **2021**, *23*, 12309-12320
- (65) Melville, J.; Hargis, C.; Davenport, M. T.; Hamilton, R. S.; Ess, D. H. Machine learning analysis of dynamic-dependent bond formation in trajectories with consecutive transition states. *J. Phys. Org. Chem.* **2022**, *35*, e4405
- (66) Bell, R. P.; Hinshelwood, C. N. The theory of reactions involving proton transfers. *Proc. Royal Soc. Lond.* **1997**, *154*, 414-429
- (67) Evans, M. G.; Polanyi, M. Inertia and driving force of chemical reactions. *J. Chem. Soc. Faraday Trans.* **1938**, *34*, 11-24
- (68) Hammond, G. S. A Correlation of Reaction Rates. J. Am. Chem. Soc. 1955, 77, 334-338
- (69) Mandal, D.; Mallick, D.; Shaik, S. Kinetic Isotope Effect Determination Probes the Spin of the Transition State, Its Stereochemistry, and Its Ligand Sphere in Hydrogen Abstraction Reactions of Oxoiron(IV) Complexes. *Acc. Chem. Res.* **2018**, *51*, 107-117
- (70) Serrano-Plana, J.; Oloo, W. N.; Acosta-Rueda, L.; Meier, K. K.; Verdejo, B.; García-España, E.; Basallote, M. G.; Münck, E.; Que, L., Jr.; Company, A.; Costas, M. Trapping a Highly Reactive Nonheme Iron Intermediate That Oxygenates Strong C—H Bonds with Stereoretention. *J. Am. Chem. Soc.* **2015**, *137*, 15833-15842
- (71) Prat, I.; Company, A.; Postils, V.; Ribas, X.; Que Jr, L.; Luis, J. M.; Costas, M. The Mechanism of Stereospecific C-H Oxidation by Fe(Pytacn) Complexes: Bioinspired Non-Heme Iron Catalysts Containing cis-Labile Exchangeable Sites. *Chem. Eur. J.* **2013**, *19*, 6724-6738

# TOC Graphic

